Geophysical Journal International

Geophys. J. Int. (2018) **215,** 1943–1961
Advance Access publication 2018 September 18
GJI Geomagnetism, rock magnetism and palaeomagnetism

doi: 10.1093/gji/ggy375

Topographic distortions of magnetotelluric transfer functions: a high-resolution 3-D modelling study using real elevation data

Johannes S. Käufl, Alexander V. Grayver and Alexey V. Kuvshinov

Department of Earth Sciences, Institute of Geophysics, ETH Zürich, 8092 *Zurich, Switzerland. E-mail: johannes.kaeufl@erdw.ethz.ch*

Accepted 2018 September 14. Received 2018 August 25; in original form 2017 October 17

SUMMARY

This study aims at quantifying the influence of topographic distortions on magnetotelluric transfer functions, including the impedance tensor, tipper and phase tensor. To this end, we performed a series of numerical experiments using real topography. We utilized a high-order 3-D finite element modelling code combined with locally refined unstructured meshes to achieve an accurate representation of topography and low modelling errors. We calculated electromagnetic fields for a region in the Hangai Mountains (Mongolia) for a wide period range and showed that, depending on the period and size of topographic features, distortions due to both galvanic and inductive effects can become significant. In addition, we quantify the effect of the vertical electric field component for tilted electric dipoles located on slopes. For real topography examples considered here, we found that galvanic distortions dominate at periods >10 s, resulting in a static shift effect. At shorter periods (<1 s), inductive effects cause significant variations of the impedance, the phase tensor and the tipper.

Key words: Electrical properties; Electromagnetic theory; Magnetotellurics; Numerical modelling.

1 INTRODUCTION

The influence of topography on magnetotelluric (MT) data has long been discussed in the literature. Early studies reported on possible significant distortions in MT transfer functions (e.g. Ku *et al.* 1973; Berdichevsky & Dmitriev 1976; Wannamaker *et al.* 1986) and associated risks of misinterpretations for derived resistivity models. Subsequent research on the topic was concentrated around methods aimed to correct for or minimize the influence of topography in the data (e.g. Groom & Bahr 1992). Jiracek (1990) noted that topographic distortions can have both galvanic and inductive origins, depending on the period and terrain roughness in the vicinity of a measurement point. This complex behaviour makes topographic effects indistinguishable from the subsurface response. Therefore, data correction methods are rarely used for real data collected on land since the topography effect is believed to take a minor part in the total variability of the responses. The extent to which this assumption is valid remains sparsely covered in the literature. Therefore, given the increasing amount of MT data collected in mountainous regions and availability of efficient modelling codes, the question of topography influence prompts a dedicated study.

The most consistent way to account for topography effect in the data is to model it. Among different electromagnetic (EM) modelling approaches, methods using unstructured and locally refined meshes appear to be the most efficient since the resulting meshes are at least linearly conforming to the air-ground interface and can have a finer mesh around topographic features and receivers. Combined with the progress in numerical methods and high-performance computing, we are currently at a stage where topography can be reliably modelled. Over the last decade, several 3-D finite element codes appeared (e.g. Nam *et al.* 2007; Schwarzbach *et al.* 2011; Ren *et al.* 2013; Usui 2015; Kordy *et al.* 2016; Jahandari *et al.* 2017), showing responses for models with topographic undulations. However, the main goal of these studies was to present and validate novel numerical schemes, hence they did not concentrate on studying topographic distortions and physical processes, which cause them, in detail.

In contrast, in this study we perform a series of numerical experiments focusing on distortions due to real complex 3-D topography of the Hangai Mountains in Mongolia. We aim to conduct a high-resolution 3-D modelling study, covering a wide frequency range where both galvanic and inductive effects are significant. The illustration of the general physical processes is done by analysing current density and charge accumulation within the model. We further address the questions of how different types of MT transfer functions are affected by realistic topography and study the effect of tilted electric dipoles located on slopes.

2 THEORY

Maxwell's equations under the quasi-static approximation form the physical basis for MT. In the frequency domain, with the time dependence expressed by $e^{+i\omega t}$, Maxwell's equations read

$$\epsilon_0 \nabla \cdot \vec{E}(\vec{r}, \omega) = q(\vec{r}, \omega) \qquad \text{(Gauss' law)} \qquad (1)$$

© The Author(s) 2018. Published by Oxford University Press on behalf of The Royal Astronomical Society.

Downloaded from https://academic.oup.com/gji/article-abstract/215/3/1943/5101445 by ETH Zürich user on 12 October 2018

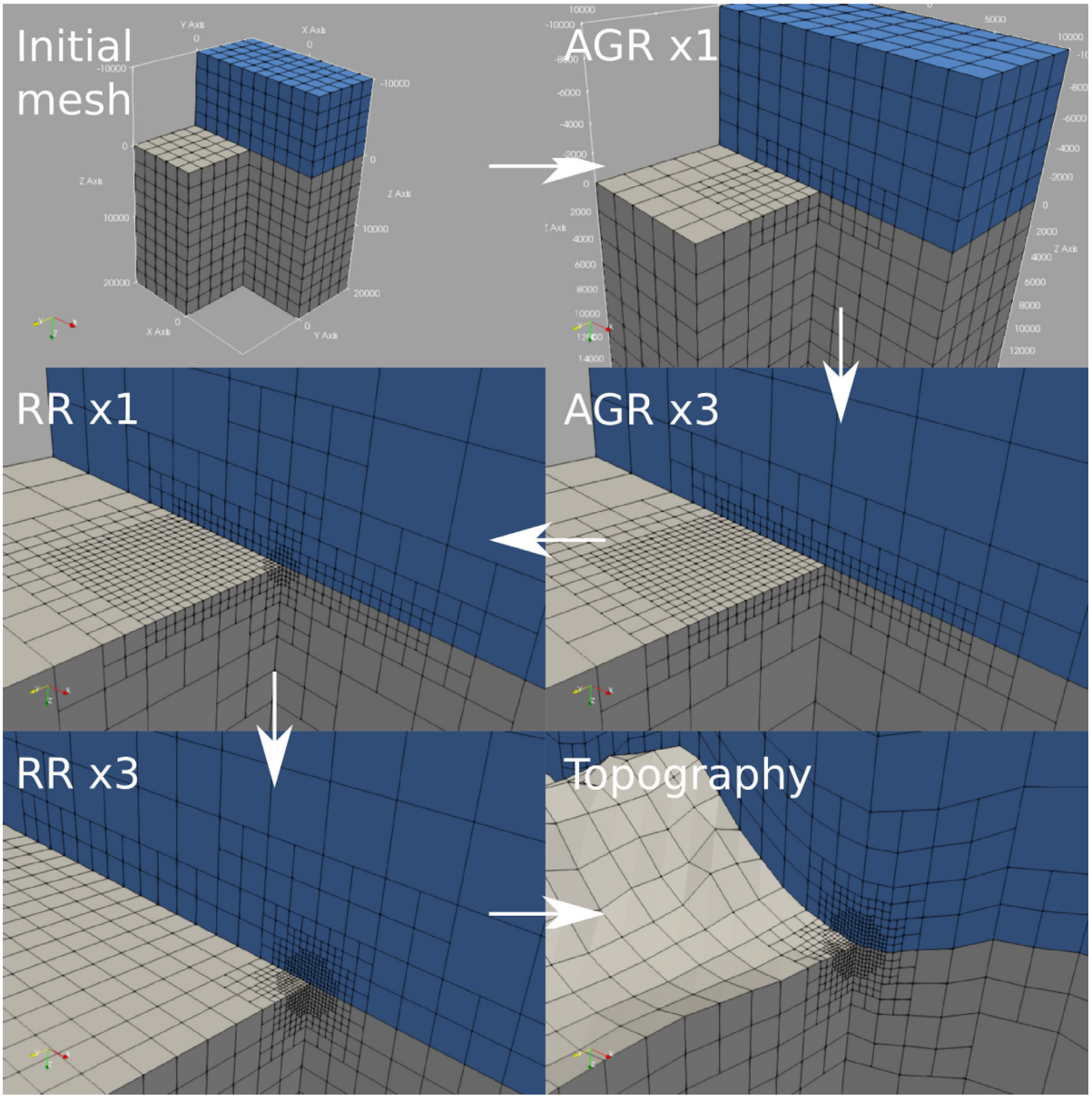

Figure 1. Example of the mesh refinement process, consisting of three steps of air-ground refinements (AGR), three refinements around a single receiver (RR) with subsequently decreasing radius, followed by the topography conforming transformation.

$$\mu_0 \nabla \cdot \vec{H}(\vec{r}, \omega) = 0 \tag{2}$$

$$\nabla \times \vec{E}(\vec{r}, \omega) = -\mathrm{i}\omega\mu_0 \vec{H}(\vec{r}, \omega) \qquad \text{(Faraday's law)} \tag{3}$$

$$\nabla \times \vec{H}(\vec{r}, \omega) = \vec{j}(\vec{r}, \omega) \qquad \text{(Ampère's law).} \tag{4}$$

Here, $\vec{H}$ is the magnetic field (H-field), $\vec{E}$ the electric field (E-field), q the charge density and $\vec{j}$ the current density. All four quantities are complex-valued functions of frequency and space $\vec{r}$. In what follows, the dependence on frequency and space will be assumed. ε_0 is the vacuum permittivity and μ_0 the vacuum permeability. Recalling Ohm's law,

$$\vec{j} = \sigma \vec{E} + \vec{j}_{\text{ext}}, \tag{5}$$

where $\sigma \equiv \sigma(x, y, z)$ denotes the real-valued conductivity and assuming zero extraneous current ($\vec{j}_{\text{ext}} = 0$) within the Earth, Ampère's law reads

$$\nabla \times \vec{H} = \sigma \vec{E}. \tag{6}$$

According to Jiracek (1990), the effect due to topography consists of inductive and galvanic components that affect EM fields and lead to distortions of MT transfer functions. To gain more insight, we express the EM field in terms of a vector potential $\vec{A}$ and a scalar potential V, corresponding to inductive and galvanic components, respectively:

$$\mu_0 \vec{H} = \nabla \times \vec{A} \tag{7}$$

$$\vec{E} = -\nabla V - \mathrm{i}\omega \vec{A}. \tag{8}$$

Downloaded from https://academic.oup.com/gji/article-abstract/215/3/1943/5101445 by ETH Zürich user on 12 October 2018

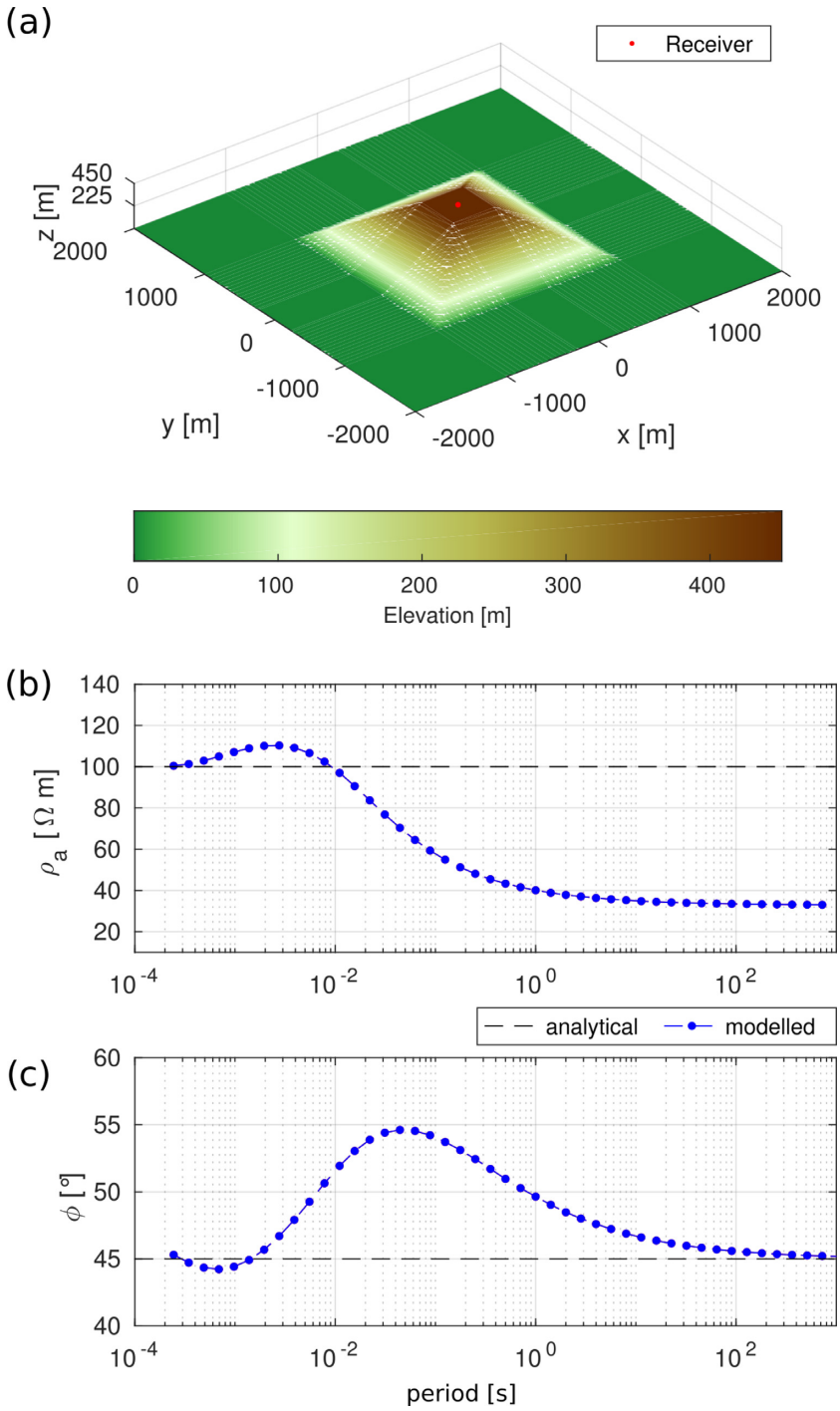

Figure 2. (a) Trapezoidal hill with a receiver located at (0, 0) on top of the hill, apparent resistivity (b) and phase (c) at the receiver. Blue curves are modelled responses and black curves the analytical solution for a model without topography. Due to the symmetry, Z_{xy} and Z_{yx} are equal.

Further, employing the Coulomb gauge ($\nabla \cdot \vec{A} = 0$), we obtain two Poisson equations,

$$\nabla \cdot \vec{E} = \nabla^2 V = -\frac{q}{\epsilon_0} \tag{9}$$

and

$$\nabla \times \vec{H} = -\nabla^2 \vec{A} = \mu_0 \vec{j}. \tag{10}$$

By taking the divergence of eq. (6), applying Gauss' law from eq. (1) and solving for q, we derive an expression of the charge density arising from conductivity gradients:

$$q = -\frac{\epsilon_0}{\sigma} \vec{E} \cdot \nabla\sigma. \tag{11}$$

Alternatively, q can be expressed in terms of the current as

$$q = -\epsilon_0 \frac{\vec{j}}{\sigma^2} \cdot \nabla\sigma = \epsilon_0 \vec{j} \cdot \nabla \frac{1}{\sigma}. \tag{12}$$

Downloaded from https://academic.oup.com/gji/article-abstract/215/3/1943/5101445 by ETH Zürich user on 12 October 2018

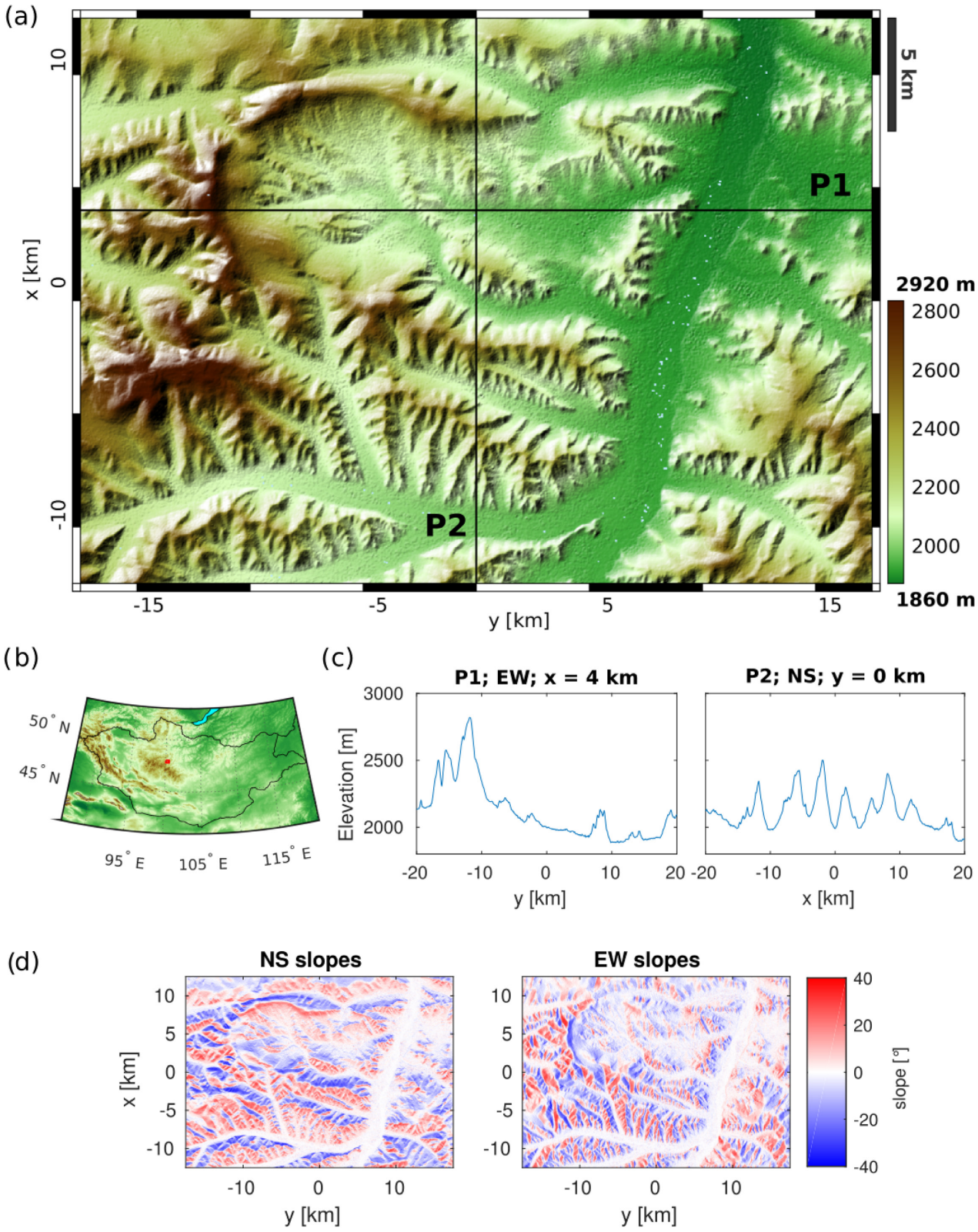

Figure 3. (a) Topographic map of the study area, black lines indicate the two profiles. (b) Location of the modelling area in Mongolia (centre: 47.9°N, 100.24°E). (c) Elevation along the profiles P1 and P2. (d) Slopes in north–south and east–west directions.

Downloaded from https://academic.oup.com/gji/article-abstract/215/3/1943/5101445 by ETH Zürich user on 12 October 2018

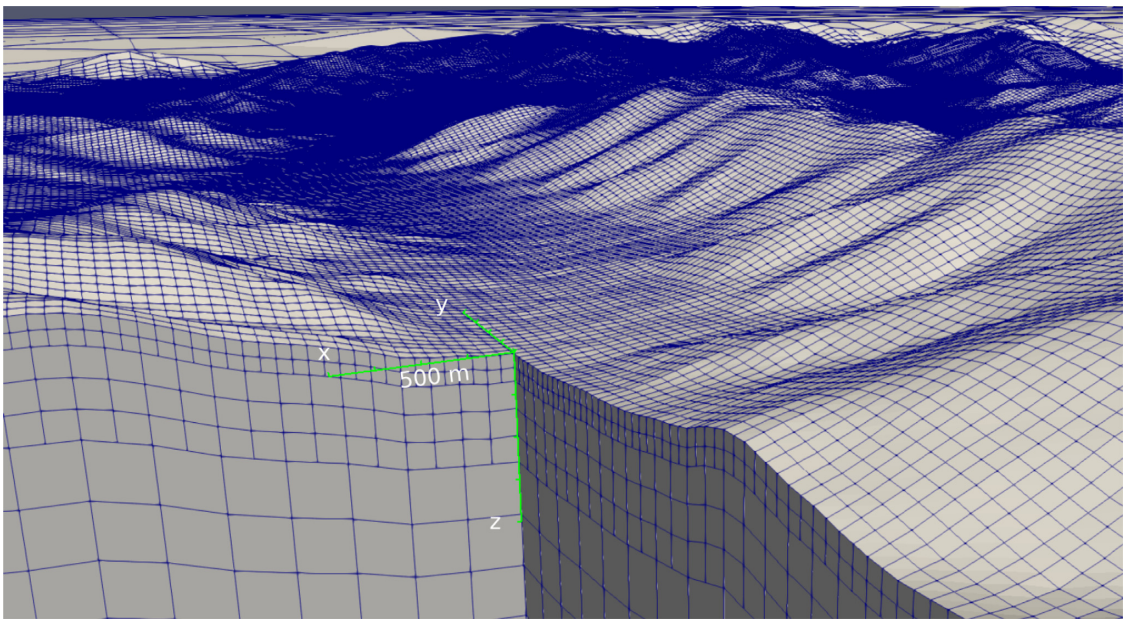

Figure 4. Part of the resulting hexahedral mesh of the study region. The coordinate axes are marked in green.

Then, the solutions to eqs (9) and (10) can be written using the Green's function as:

$$V(\vec{r},\omega) = \frac{1}{4\pi}\iiint \frac{\vec{j}(\vec{r}\,',\omega)\cdot\nabla\left(\sigma(\vec{r}\,')^{-1}\right)}{|\vec{r}-\vec{r}\,'|}\,\mathrm{d}^3r' \tag{13}$$

and

$$\vec{A}(\vec{r},\omega) = \frac{\mu_0}{4\pi}\iiint \frac{\vec{j}(\vec{r}\,',\omega)}{|\vec{r}-\vec{r}\,'|}\,\mathrm{d}^3r'. \tag{14}$$

Eqs (13) and (14) show that both scalar and vector potentials are proportional to the current. However, for the electric field, the vector potential is further scaled by the frequency (see eq. 8). As a result, the galvanic term will become dominant as frequency decreases (Singer 1992).

Eqs (9), (11) and (13) reveal that charges accumulate at conductivity contrasts, which affects the E-field and causes so called galvanic distortions of the impedance, as was repeatedly described by various authors (Jones & Price 1970; Singer 1992, among others). There is a consensus that galvanic distortions of the impedance tensor $\mathbf{Z}(\vec{r},\omega)$ can be represented as a product of the undistorted impedance $\mathbf{Z}'(\vec{r},\omega)$ with a 2×2 distortion tensor $\mathbf{D}(\vec{r})$,

$$\mathbf{Z}(\vec{r},\omega) = \mathbf{D}(\vec{r})\mathbf{Z}'(\vec{r},\omega), \tag{15}$$

where

$$D = \begin{pmatrix} D_{xx} & D_{xy} \\ D_{yx} & D_{yy} \end{pmatrix} \tag{16}$$

is real valued and does not depend on frequency. It is further assumed that $\mathbf{D}$ is not singular.

For a 2-D conductivity distribution (taking $\partial_x\sigma = 0$), we have $Z_{xx} = Z_{yy} = 0$ and

$$Z_{||}(\vec{r},\omega) = D_{xy}(\vec{r})Z'_{xy}(\vec{r},\omega) \tag{17}$$

$$Z_{\perp}(\vec{r},\omega) = D_{yx}(\vec{r})Z'_{yx}(\vec{r},\omega), \tag{18}$$

resulting in a static (i.e. frequency independent) shift of the apparent resistivity, with the phase of Z unaffected. The same is, obviously, valid for any 1-D conductivity distribution. In a 3-D case, as it is evident from eq. (15), both the apparent resistivity and the phase of Z are generally affected, moreover the apparent resistivity shows a more complex behaviour rather than a (static) shift.

Further, the (total) electric and magnetic fields can be split into primary and secondary parts as

$$\vec{E} = \vec{E}_\mathrm{p} + \vec{E}_\mathrm{s} \tag{19}$$

$$\vec{H} = \vec{H}_\mathrm{p} + \vec{H}_\mathrm{s}. \tag{20}$$

Primary (also called normal or background) fields $\vec{E}_\mathrm{p}$ and $\vec{H}_\mathrm{p}$ represent the fields induced in a layered 1-D conductivity model $\sigma_{\text{1-D}}(z)$. For a plane-wave source, the vertical component of the primary EM field is zero. Secondary (also called anomalous or scattered) fields $\vec{E}_\mathrm{s}$ and $\vec{H}_\mathrm{s}$ are a superposition of fields generated by inductive and galvanic effects due to lateral conductivity variations ($\sigma - \sigma_{\text{1-D}} \neq 0$). For the homogeneous subsurface model we consider in this paper, secondary fields result entirely from the effects due to topography.

Let us now consider a medium with two homogeneous regions with conductivities σ_1 and σ_2 ($\sigma_2 > \sigma_1$). For this model, the volume charge density (eq. 11), can be replaced by the surface charge density

$$q_\mathrm{S}(\vec{r}_\mathrm{I}) = -\epsilon_0\,\frac{\sigma_2-\sigma_1}{\sigma_2}\,\vec{E}(\vec{r}_\mathrm{I})\cdot\hat{n}(\vec{r}_\mathrm{I}), \tag{21}$$

at a position $\vec{r}_\mathrm{I}$ on the interface (Jiracek 1990). Here, $\hat{n}(\vec{r}_\mathrm{I}) = \langle n_x, n_y, n_z\rangle$ denotes the surface normal on the interface, pointing towards the region with a higher conductivity. Separating $\vec{E}$ according to eq. (19), introducing $\hat{n}_\mathrm{H} = \langle n_x, n_y, 0\rangle$ to account for the deviation of the interface from a horizontal plane, and assuming the dependence on $\vec{r}_\mathrm{I}$, yields

$$q_\mathrm{S} = -\epsilon_0\,\frac{\sigma_2-\sigma_1}{\sigma_2}\,(\vec{E}_\mathrm{p}\cdot\hat{n}_\mathrm{H} + \vec{E}_\mathrm{s}\cdot\hat{n}). \tag{22}$$

The equations above reveal several aspects:

(1) Since $\sigma_\mathrm{air} \ll \sigma_\mathrm{Earth}$, the ratio $\frac{\sigma_\mathrm{Earth}-\sigma_\mathrm{air}}{\sigma_\mathrm{Earth}} \approx 1$ for most terrains.

Downloaded from https://academic.oup.com/gji/article-abstract/215/3/1943/5101445 by ETH Zürich user on 12 October 2018

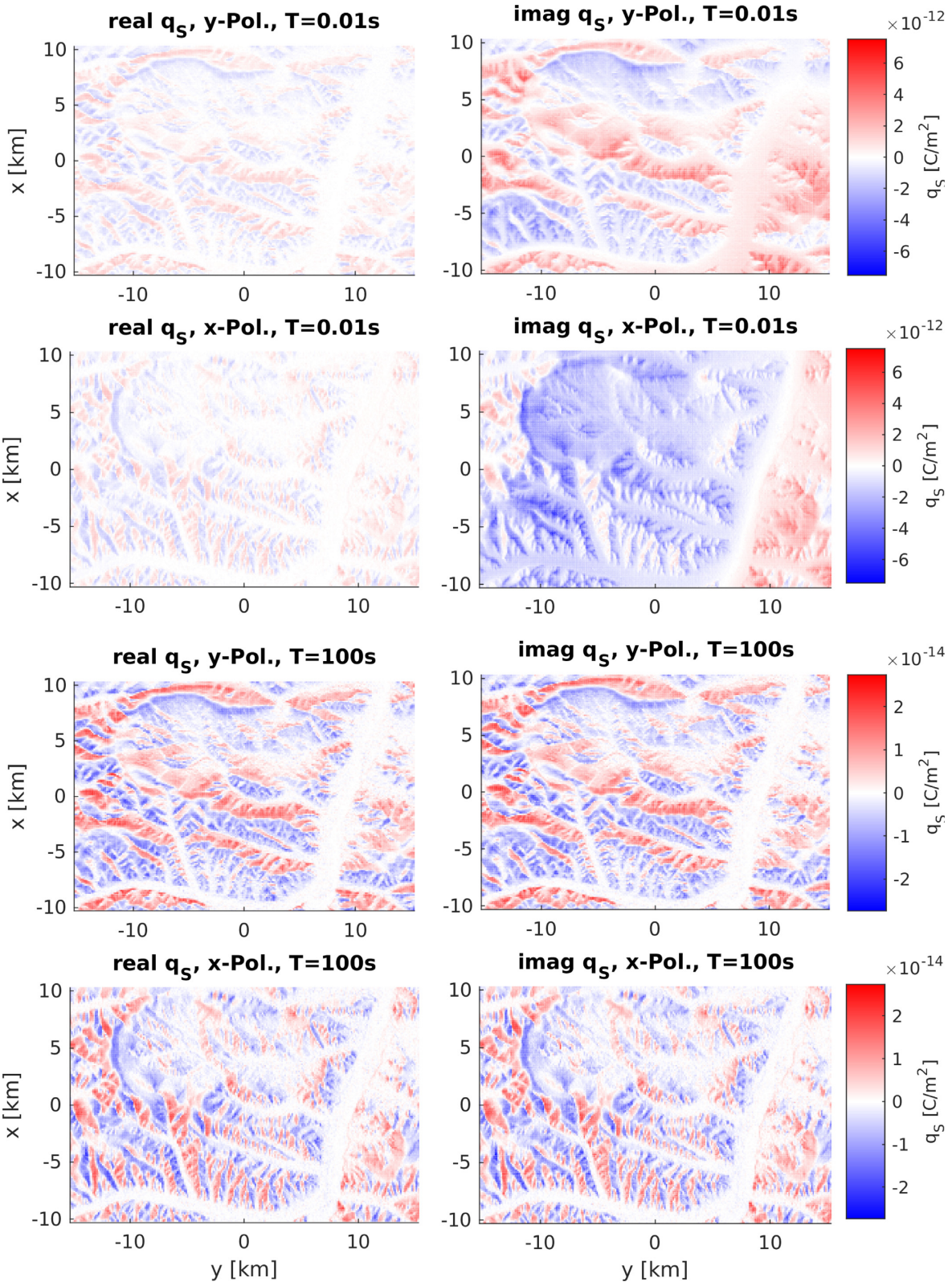

Figure 5. Surface charge density for the *y*-polarized (first and third rows) and *x*-polarized (second and fourth rows) incident plane wavefields (see eqs 25 and 26) for periods of 0.01 s (upper four panels) and 100 s (lower four panels).

Downloaded from https://academic.oup.com/gji/article-abstract/215/3/1943/5101445 by ETH Zürich user on 12 October 2018

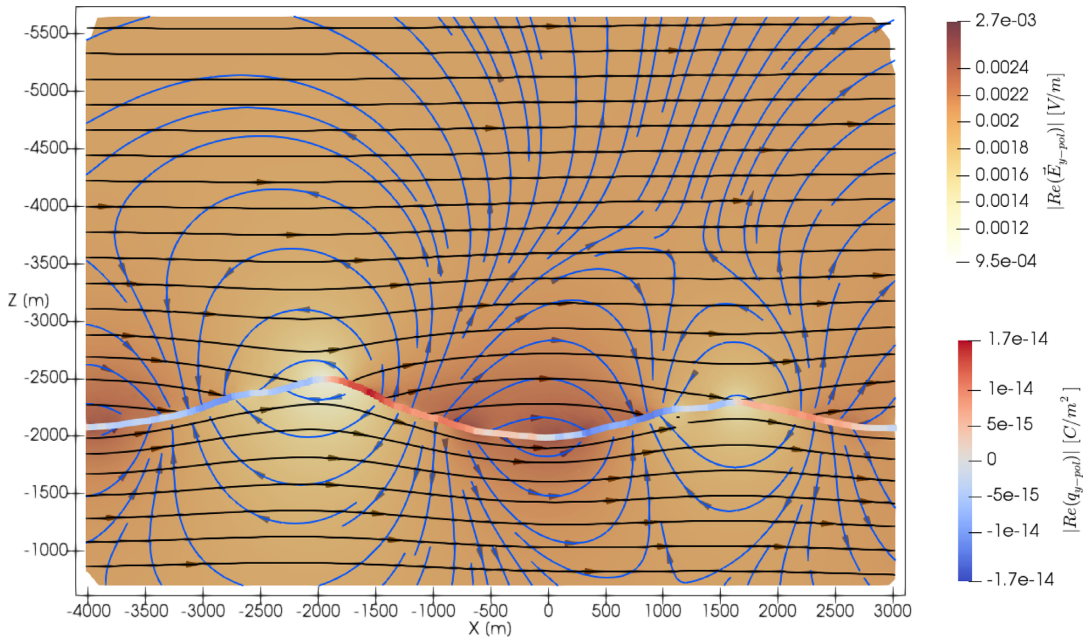

Figure 6. Real parts of the electric field and surface charge density shown in a vertical plane along the central part of P2 for the period of 100 s. The streamlines represent the direction of the fields in the *xz*-plane, black for the total and blue for the secondary electric fields (eq. 19), respectively. Since both the electric field and the charge density have a phase of ≈45° (see Figs A4 and 5), we plot only real parts here.

(2) The dot product in eq. (21) determines the sign of the charges. If the angle between $\vec{E}$ and $\hat{n}$ is within the range $(-90°, 90°)$ negative charges accumulate, whereas positive charges accumulate otherwise.

(3) Terms on the right-hand side of eq. (22) indicate that the steepness of the slope is an important factor for the accumulation of charges. Therefore, even spatially small, but steep topographic features can lead to significant distortions.

Although the analysis presented above may give some insight into the causes for topographic distortions of MT data, one sees that the interplay between galvanic and inductive effects and the complexity of real topography necessitate a rigorous 3-D numerical modelling to properly quantify the effect on MT transfer functions. In the following sections we address this problem.

3 METHODOLOGY

We will present an analysis of the topography effect on the following MT transfer functions:

(1) impedance tensor, **Z**, conventionally visualized in the form of apparent resistivity, ρ_a, and phase, ϕ (as described e.g. by Berdichevsky & Dmitriev 2002);

(2) the vertical magnetic transfer functions or tipper, **T** (as described e.g. by Berdichevsky & Dmitriev 2008);

(3) phase tensor Φ visualized as ellipses showing the ellipticity, strike angle θ and normalized skew Ψ (as described by Caldwell *et al.* 2004; Booker 2014).

We calculate these responses for an Earth model with topography and a homogeneous subsurface resistivity of $\rho_h = 100\ \Omega$m. The resistivity of the air was set to $10^9\ \Omega$m. Differences between modelled and analytical responses (as obtained in a flat Earth model with homogeneous resistivity) are thus assumed to be caused by topography.

To calculate EM fields, the following equation is solved:

$$\nabla \times (\mu_0^{-1} \nabla \times \vec{E}) + \mathrm{i}\omega\sigma \vec{E} = 0 \qquad \text{in} \quad \Omega. \tag{23}$$

Here, ΩR^3 is the modelling domain and $\vec{E}$ the total E-field. Further, the inhomogeneous Dirichlet boundary conditions,

$$\vec{E} = \vec{E}_0 \quad \text{on} \quad \partial\Omega \tag{24}$$

are applied, where $\vec{E}_0$ results from the solution of 2-D Maxwell's equations on the boundaries. Solutions for two orthogonal source polarizations are computed. The primary plane wavefields for two polarizations are defined as

$$y\text{-polarization} \quad \begin{cases} \vec{H}_p = \langle 0, 1, 0 \rangle \\ \vec{E}_p = \langle Z_{1\text{-D}}, 0, 0 \rangle \end{cases} \tag{25}$$

and

$$x\text{-polarization} \quad \begin{cases} \vec{H}_p = \langle 1, 0, 0 \rangle \\ \vec{E}_p = \langle 0, -Z_{1\text{-D}}, 0 \rangle. \end{cases} \tag{26}$$

The 3-D finite element code GoFEM (Grayver & Kolev 2015) was used to solve eq. (23) numerically. In order to improve accuracy of the numerical solutions and to discretize topography accurately, we used second-order Nédélec elements and locally refined unstructured meshes. The resulting models consisted of up to 120 millions of unknowns and required scalable parallel solvers. To make the solution of these systems feasible, we used a parallel iterative FGMRES solver and auxiliary-space multigrid preconditioner as described in Grayver & Kolev (2015).

Discretization of the modelling domain Ω was done by using hexahedral elements. The mesh generation methodology adopted in this study consists of several steps. An initially coarse mesh, consisting of a dozen of rectangular cells in each direction, is refined within the region of interest by bisecting cells in three dimensions. The refinement cycles are performed across the air-ground interface and close to receivers where fields are sampled. This local refinement provides a trade-off between computational cost and numerical accuracy. The mesh is then adapted to the topography by a variant

Downloaded from https://academic.oup.com/gji/article-abstract/215/3/1943/5101445 by ETH Zürich user on 12 October 2018

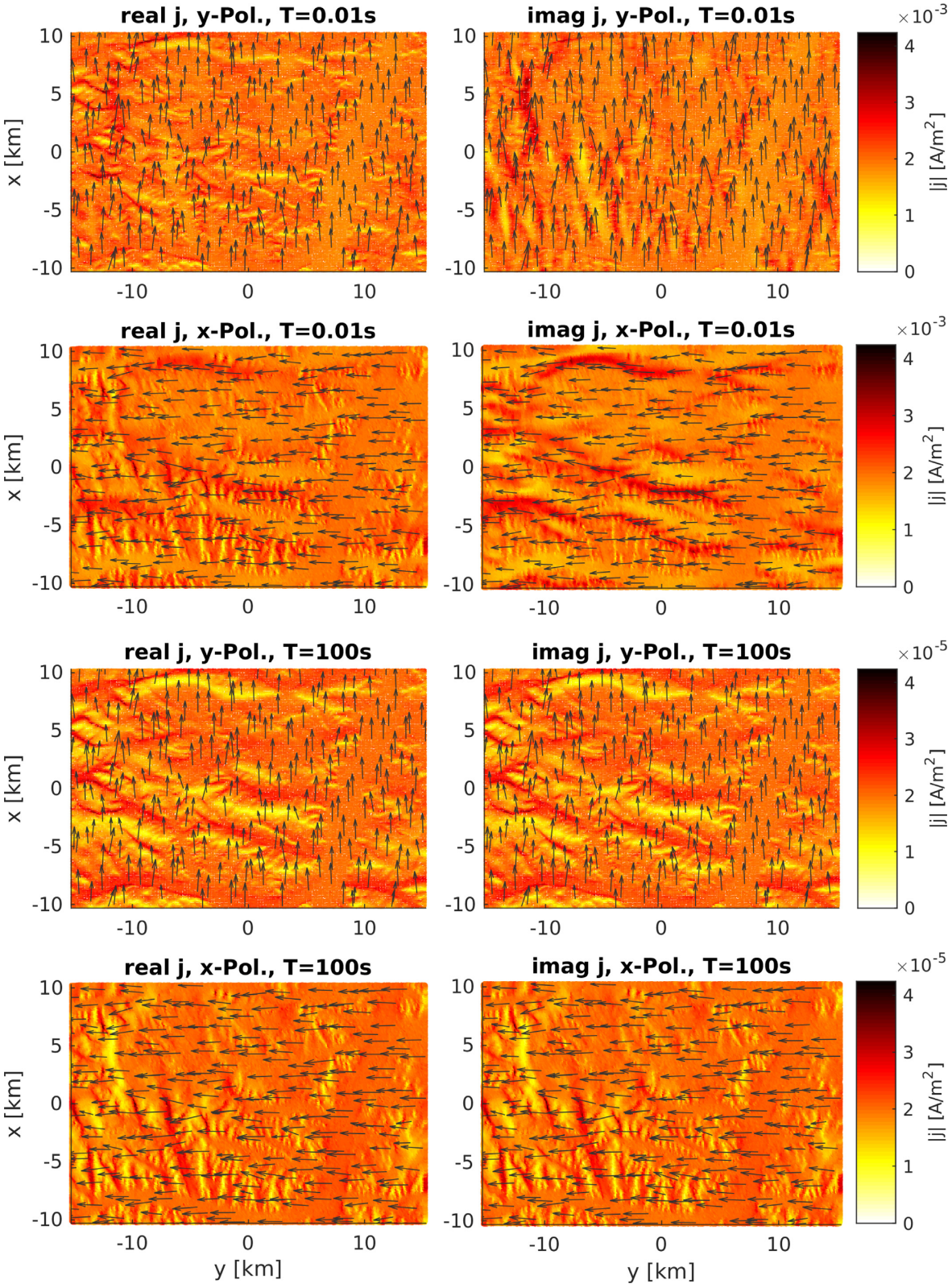

Figure 7. Magnitude and direction of the total current density at the surface for the *y*-polarized (first and third rows) and *x*-polarized (second and fourth rows) incident plane wavefields (see eqs 25 and 26) for periods of 0.01 s (upper four panels) and 100 s (lower four panels).

Downloaded from https://academic.oup.com/gji/article-abstract/215/3/1943/5101445 by ETH Zürich user on 12 October 2018

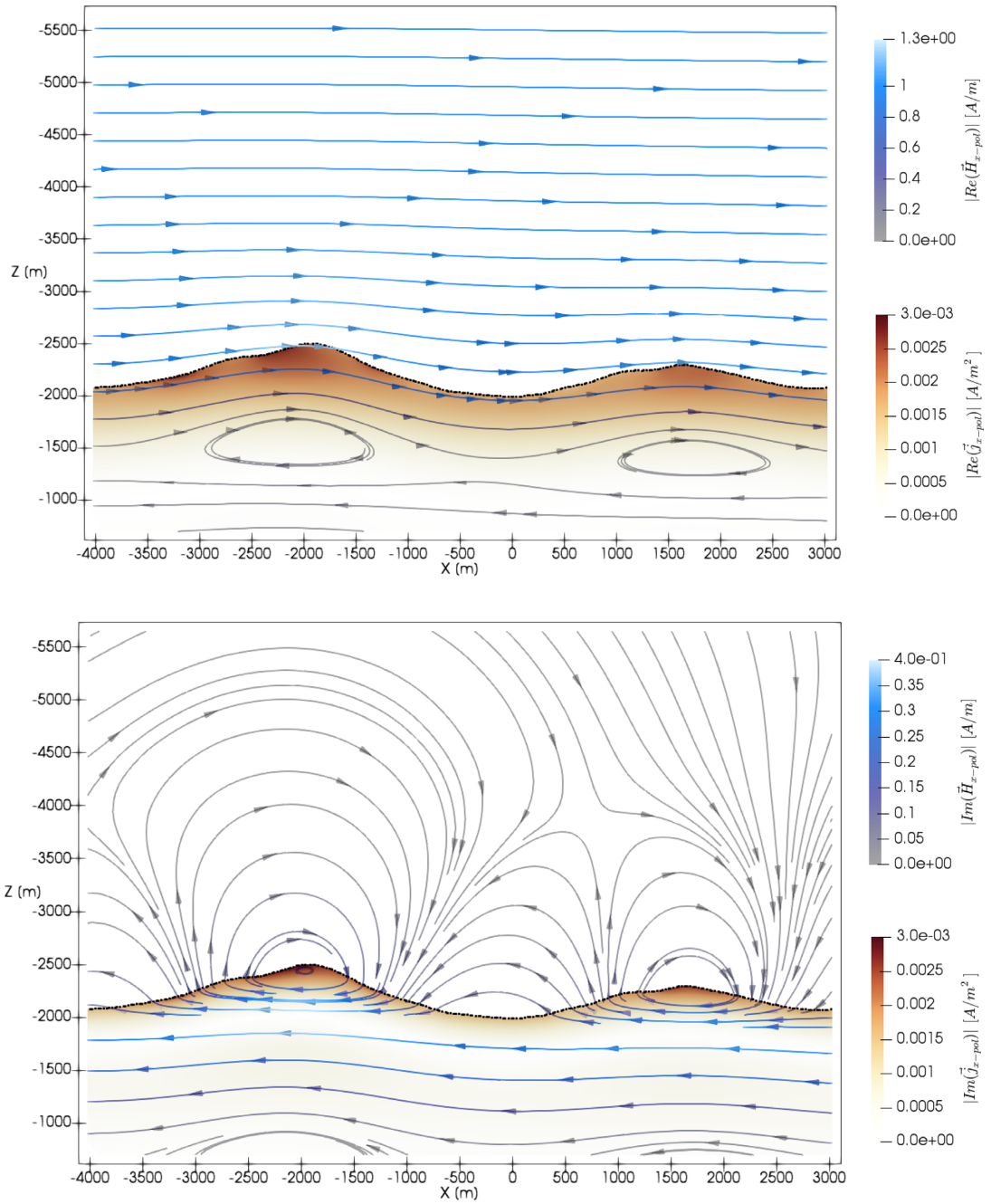

Figure 8. Real (top) and imaginary (bottom) parts of the current density and $\vec{H}$ at a period of 0.01 s in a vertical plane along the central part of P2. Streamlines represent the direction of the total H-field in the *xz*-plane and their colour the magnitude of the 3-D vector.

of surface conformal transfinite interpolation, which keeps domain boundaries flat, while distorting cells within domain to ensure they conform (within the discretization error) to the topography. Fig. 1 illustrates the process.

4 RESULTS

4.1 Synthetic topography

We first consider a simple synthetic case in order to illustrate the interplay between galvanic and inductive effects. Specifically, MT transfer functions were calculated for a wide frequency range in the model of a trapezoidal hill used by several authors (Nam *et al.* 2007; Ren *et al.* 2013; Kordy *et al.* 2016, among others) to validate their codes. The hill is depicted in Fig. 2 and has a square base with a length of 2000 m, a height of 450 m and a flat 450 $\times$ 450 m^2 top. Fig. 2 shows apparent resistivity and phase values for a receiver located at (0, 0) on top of the hill. Clearly, galvanic distortions dominate at long periods (>10 s): phases are $\approx$45°, whereas values for ρ_a are shifted by a value which remains nearly constant across periods. In contrast, inductive effect prevail for periods between 0.001 and 1 s. In this period range, both phase and apparent resistivity exhibit a frequency-dependent behaviour. For shorter periods, transfer functions attain half-space values.

Downloaded from https://academic.oup.com/gji/article-abstract/215/3/1943/5101445 by ETH Zürich user on 12 October 2018

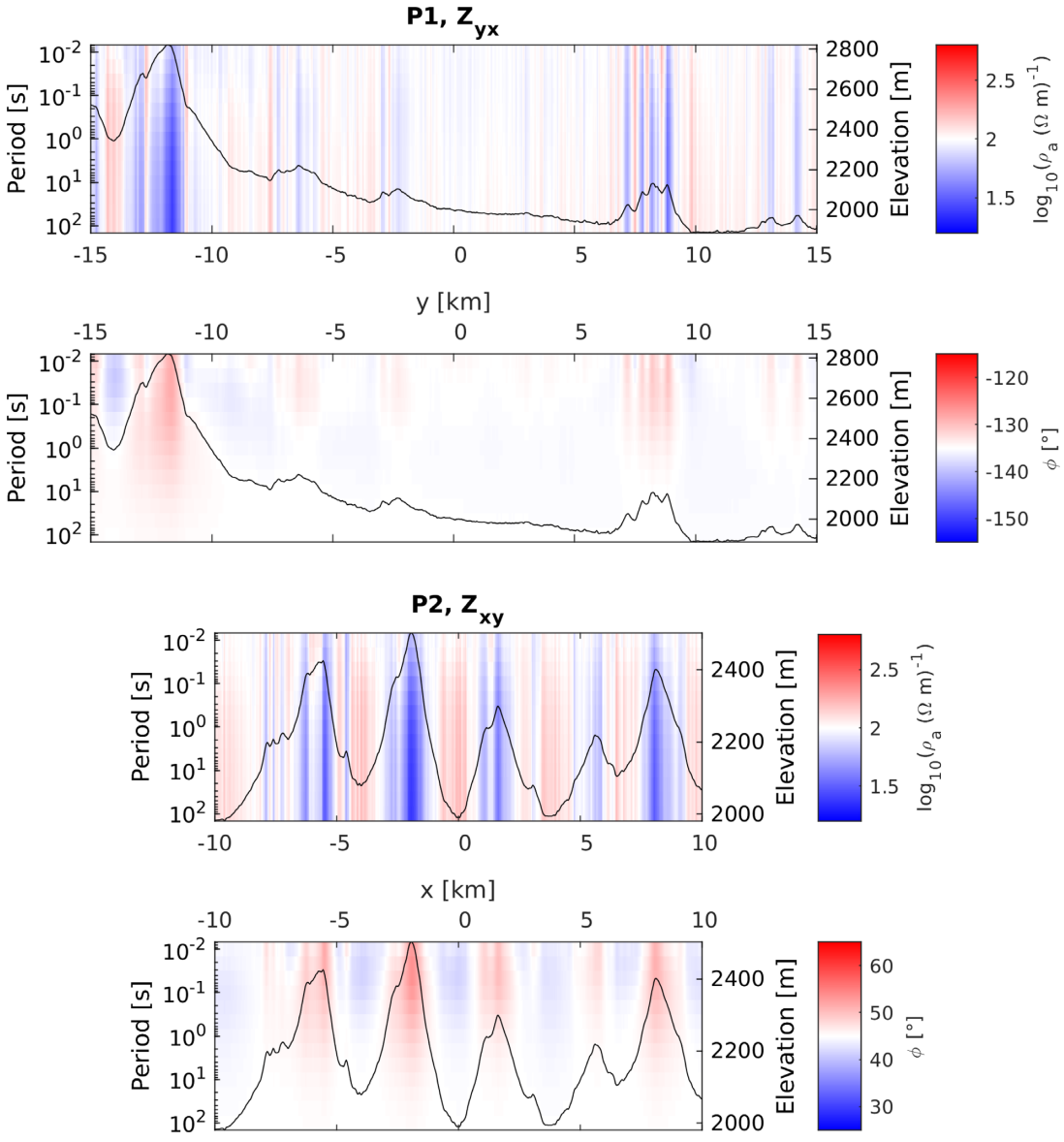

Figure 9. Apparent resistivity and phase pseudo-sections of the *xy*- and *yx*-components along the profiles P1 and P2 (see Fig. 3a). A solid black line depicts the elevation.

4.2 Real topography

To quantify the influence of realistic topography, we computed transfer functions for a high-resolution model of a region in the Hangai Mountains, Mongolia. This region was chosen since we, in collaboration with University of Münster, recently conducted a 3-D MT survey in the Hangai Mountains and adjacent regions (for results from subset of the data, see Comeau *et al.* 2018). Similar to the synthetic model, the subsurface resistivity was set to 100 Ωm. The grid of receivers has a spacing of 20 m and spans an area of 20 × 30 km^2. Fig. 3(a) shows a topographic map of the model area with two profiles (P1 and P2) used later in the study and Fig. 3(b) shows the geographic location of the model area (small red square) with respect to Mongolia. The topography has a difference of 1000 m in altitude and hosts a wide river valley in the east as well as an open crater-shaped structure located in the northwest. The intersection of P1 and P2 exhibits relatively little topography in *y*-direction and significant topography in *x*-direction. P1 crosses a large mountain in the west and the river valley in the east, while P2 crosses east–west running mountain ridges with deep valleys between. As is shown in Fig. 3(d), the slopes reach angles of up to ±30° in north–south and east–west directions.

The discrete model has an extent of 200 × 200 × 300 km^3. The initial mesh consisted of 10 × 10 × 15 cubic cells and was refined twice at the air-ground interface followed by seven receiver refinements with subsequently decreasing radius and the topography conformal transformation. The final mesh (see Fig. 4) consisted of more than two million cells, whereby the smallest cells in the central 20 × 30 km^2 region have an edge length of approximately 38 m. The topographic data with a resolution of 1 arcsec (approx. 30 m) were taken from the SRTM digital elevation model (NASA JPL 2013). Combined with the second-order Nédélec elements, the resulting problem had 100 millions of unknowns and was solved on the new CSCS Piz Daint cluster. Besides the transfer functions, charge and

Downloaded from https://academic.oup.com/gji/article-abstract/215/3/1943/5101445 by ETH Zürich user on 12 October 2018

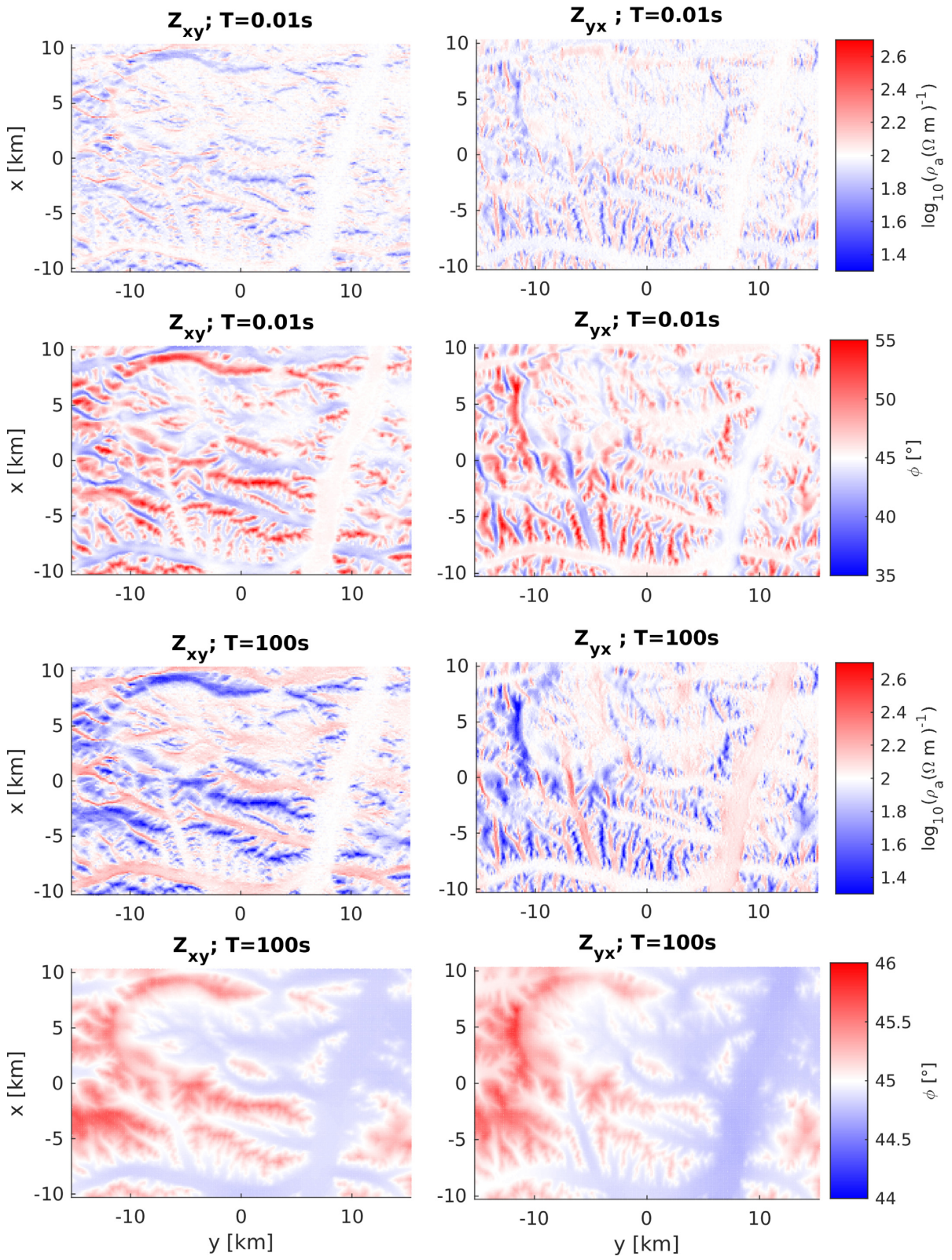

Figure 10. Map view of apparent resistivity and phase values (ϕ_{yx} was shifted to the first quadrant) for periods of 0.01 s (top half) and 100 s (bottom half). Note the different scales for phases.

Downloaded from https://academic.oup.com/gji/article-abstract/215/3/1943/5101445 by ETH Zürich user on 12 October 2018

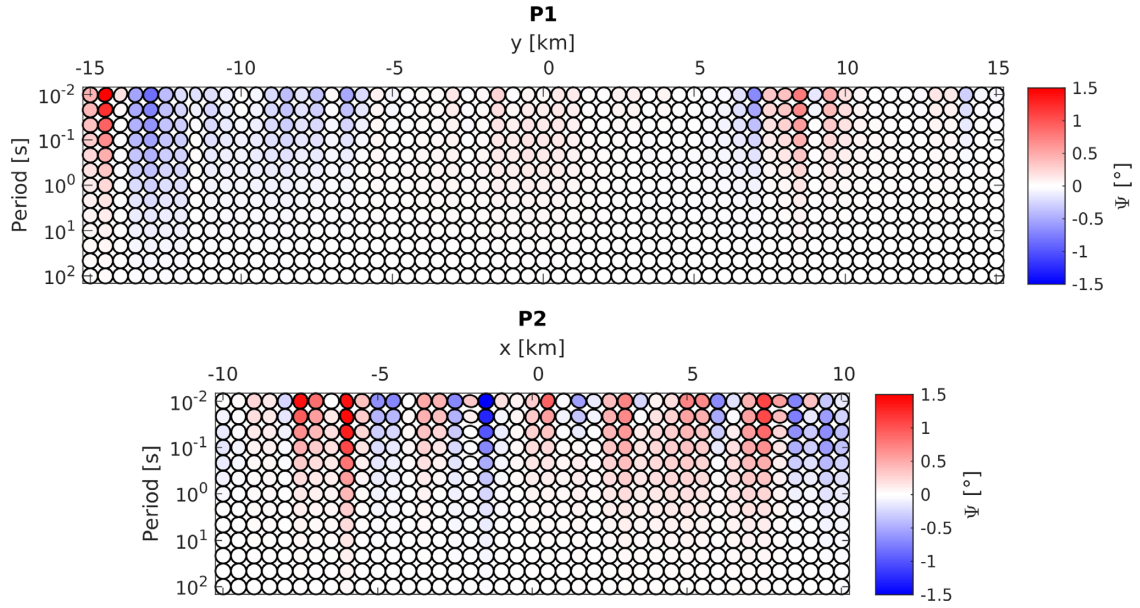

Figure 11. Pseudo-sections of phase tensor ellipses along P1 and P2 (see Fig. 3a), coloured using the normalized skew angle values.

current densities were computed at the surface to gain an insight in the physical processes.

4.2.1 *Charge density*

Fig. 5 shows the surface charge density at the air-ground interface, calculated from the modelled solution for $\vec{E}$ (*cf.* eq. 23) with eq. (21). As revealed by eq. (22), charges accumulate on slopes. For the *y*-polarization (see eq. 25), where the primary E-field points northwards, northern slopes host positive charges and southern slopes negative charges. For the *x*-polarization (see eq. 26), positive charges accumulate on the western and negative charges on the eastern slopes, respectively. For the period of 100 s, the real and imaginary parts of q_S have equal amplitudes, indicating a phase of 45°. Interestingly, the map of the charge density at 100 s is practically indistinguishable from the map of the slopes (Fig. 3d), with dense charges on slopes and zero charges at high and low points of the topography. The secondary electric field at 100 s is shown with blue streamlines in Fig. 6. It is in phase with the primary field (*cf.* Figs A4 and 5, the real and imaginary parts of $\vec{E}$ have virtually equal amplitudes) and resembles an E-field generated solely by the surface charge density according to eq. (9). This indicates that $\vec{E}_s$ is dominated by galvanic effects due to the surface charges, while inductive effects are negligible. Whenever the direction of primary and secondary fields coincide (such as in valleys), we see an increased amplitude of the total electric field. However, when primary and secondary fields are antiparallel, the total field becomes weaker (such as on top of the hills). In contrast to the electric field, the magnetic field for the period of 100 s appears virtually unaffected by the topography (*cf.* Figs A3 and A4). Thus, for long periods only amplitudes of the E-field show significant effects due to topography. Therefore, this behaviour leads to galvanic distortions of the impedance resulting in a static shift effect.

Looking at a shorter period of 0.01 s, the charge density changes notably. Clearly, the imaginary part of the charge density (Fig. 5) is considerably larger than the corresponding real part, indicating significant induction effects. Interestingly, the imaginary part of q_S is mainly affected by the large-scale topography and appears like a spatially low-pass filtered image of the slope angles. To better understand the nature of the inductive effects responsible for this behaviour, we analyse the current density in the following section.

4.2.2 *Current density*

The map of current densities at the surface is shown in Fig. 7. For the period of 100 s, the real and imaginary parts of the current density are essentially equal and exhibit a similar behaviour when compared with the charge densities from Fig. 5.

For the period of 0.01 s, the patterns in the magnitude of the current density are significantly different from the surface charge distribution. This can be explained by the fact that in addition to currents due to surface charges, there are also significant electric currents because of EM induction at this period. This can be further observed by looking at the current density and magnetic field streamlines shown in Fig. 8. Since the primary magnetic field is real valued in the air, streamlines of the imaginary part of the total magnetic field essentially show the secondary field with characteristic curls forming around mountains. This suggests that strong EM currents flow along the ridges. Indeed, one can see from the upper four panels in Fig. 7 that the highest current densities occur on peaks, thereby depicting the current channelling effect. Specifically, the maxima and minima in the imaginary part are oriented along topographic features which are perpendicular to the primary H-field direction. Furthermore, since real and imaginary parts of the current density at this period differ significantly, they affect the phase of $\vec{E}$ and, as a consequence, the phase of the impedance tensor **Z**. We can expect a clockwise shift in valleys and a counter-clockwise shift on mountain tops.

4.2.3 *Transfer functions*

Pseudo-sections of the *xy*- and *yx*-components of apparent resistivities and phases along the profiles P1 and P2 (Fig. 9) show a close correlation between the topography and the deviations of ρ_a and ϕ from the half-space values ($\rho_a = 100\,\Omega$m, $\phi_{yx} = -135°$ and $\phi_{xy} = 45°$). The apparent resistivity values lie between 12 and 209 Ωm,

Downloaded from https://academic.oup.com/gji/article-abstract/215/3/1943/5101445 by ETH Zürich user on 12 October 2018

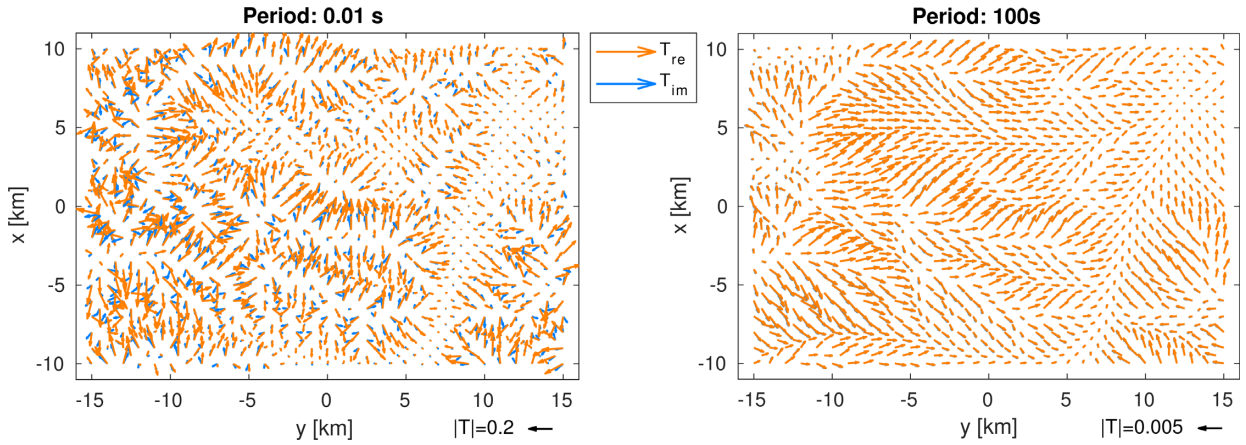

Figure 12. Maps with tipper vectors (Wiese convention) for periods of 0.01 and 100 s.

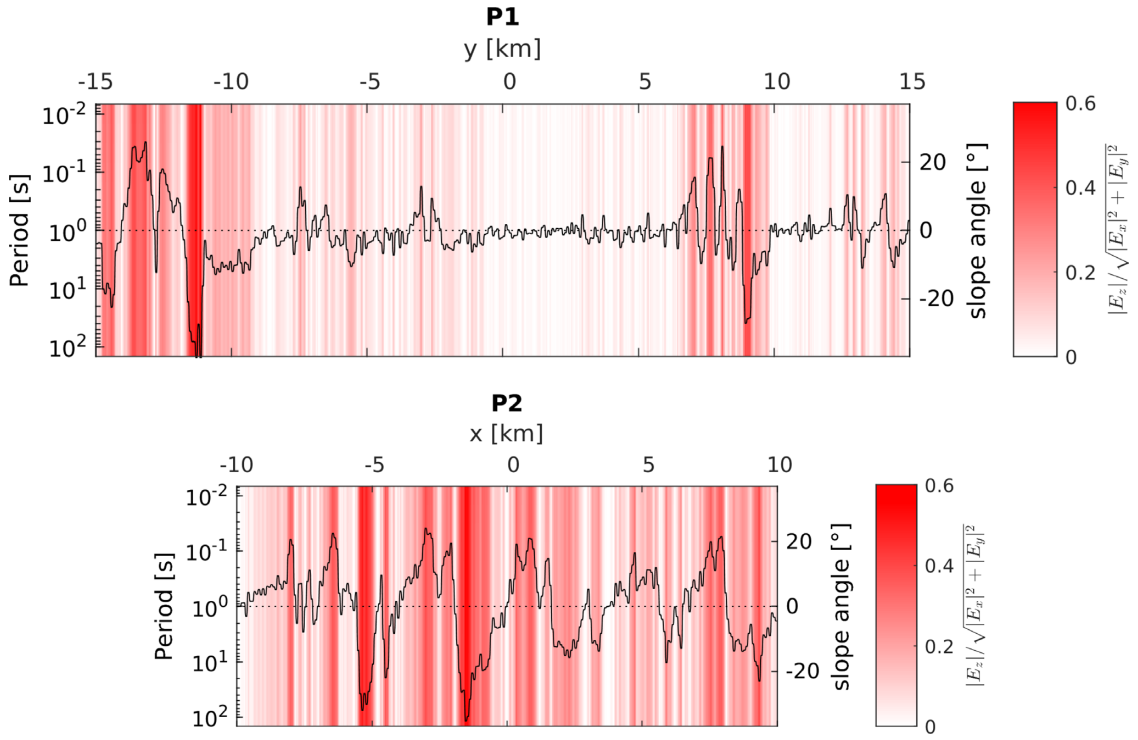

Figure 13. Pseudo-sections for profiles P1 and P2 (see Figs 3a and b) with the ratio of the vertical to the horizontal E-field. The polarizations with $\vec{E}_p$ parallel to the profile directions were used. The slope angle at the receiver location is plotted in black (right y-axis).

with 98 per cent of the values falling in the range [35, 165] Ωm. The phases show differences from -8° to $+13^\circ$, with 98 per cent being in the interval of $\pm 4^\circ$ relative to the undistorted value. Following conclusions from previous sections, ρ_a is shifted to higher values in valleys, while the phase is distorted clockwise. On hilltops, ρ_a and ϕ are shifted in the opposite way. The magnitude of the distortions depends on the steepness of the adjacent slopes (as predicted by eq. 22). Further, the period range where inductive effects dominate depends on the scale of the topographic undulations. The maximum of the phase distortion occurs at periods between 0.01 and 0.1 s, while sizeable phase distortions for the narrower valleys and peaks are confined to periods smaller than 0.1 s, the larger topographic features cause fairly large distortions in phases down to periods of 1 s and even 10 s for the peak at $y = -12$ km on P1. Results for P1 show that the topographic distortions are a local effect, the central part ($x = 0$ km) is unaffected by the hills and mountains more than 5 km away. Furthermore, it is the direction of the gradient of the topography that plays a major role. For instance, at the intersection of P1 and P2 (at $x = 4$ km and $y = 0$ km, see Fig. 3a), where the valley is oriented in y-direction, Z_{yx} remains unaffected (see P1 at $y = 0$ in Fig. 9), whereas Z_{xy} is significantly distorted (see P2 at $x = 4$ km in Fig. 9).

A map view of ρ_a and ϕ for periods of 100 and 0.01 s is given in Fig. 10. As anticipated from the charge density (Fig. 5), the distortions in Z_{xy} correlate with the east–west oriented topographic features and Z_{yx} with north–south oriented features, respectively. While both ρ_a and ϕ are affected for the period of 0.01 s, phase values exhibit little effect for the period of 100 s.

Fig. 11 shows pseudo-sections of the phase tensor ellipses along the two profiles. Since the phase tensor is not affected by galvanic

Downloaded from https://academic.oup.com/gji/article-abstract/215/3/1943/5101445 by ETH Zürich user on 12 October 2018

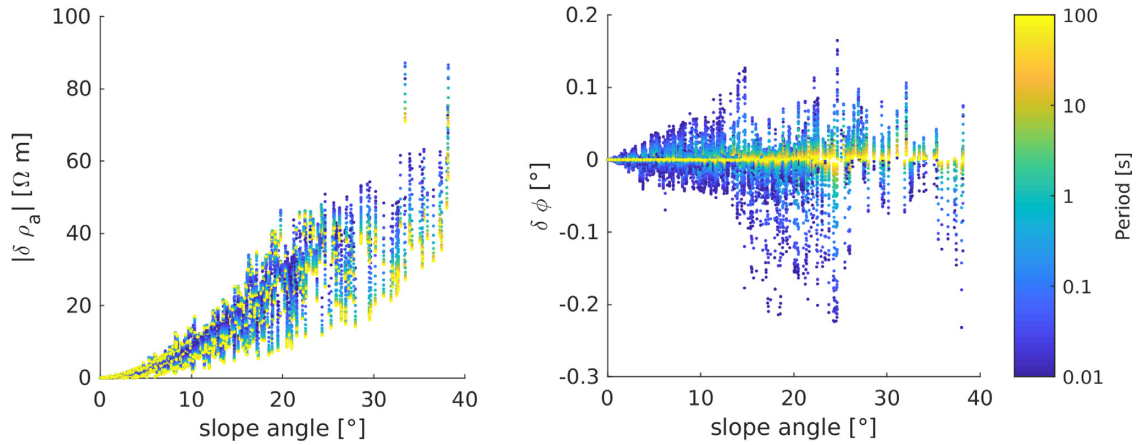

Figure 14. The effect of tilted dipoles on apparent resistivity and phase as a function of the slope angle in profile direction at the receiver location. $|\delta\rho_a|$ and $\delta\phi$ are the differences between the apparent resistivity and phase for impedances calculated using horizontal electric fields and fields tangential to the slope. Here, the differences along P1 and P2 are shown, with the Z_{xy} component used for profile P2 and the Z_{yx} component for profile P1.

distortions, the ellipses for longer periods are circles with a normalized skew angle of $\Psi = 0°$. For shorter periods, some show a notable ellipticity, reflecting the direction of the adjacent topography and a non-zero skew Ψ. With a maximum of 1.5°, Ψ stays below the threshold commonly assumed to indicate significant 3-D effects (Booker 2014).

Tipper vectors are plotted in Fig. 12 for periods of 0.01 and 100 s using the Wiese convention (pointing away from conductors; Berdichevsky & Dmitriev 2008). Clearly, they point away from the mountains at both periods, with the real part being approximately parallel to the local topography gradient. The tipper magnitudes for 0.01 s are significant, although the effect is local and strongest for sites located on or close to steep slopes. In the flatter parts of the model, the tippers are small. The magnitude of the tipper vectors at a period of 100 s is considerably smaller and practically negligible, but their direction is sensitive to the topography in a wider radius of approximately 5 km.

4.2.4 *Effects of the vertical electric fields on slopes*

In the previous section, the horizontal electric field was used to compute transfer functions. However, field data acquired in mountainous terrains cannot always use perfectly horizontal electric dipoles. Long dipole lengths (often up to 100 m) and uneven terrain may result in electric field recordings that are not truly horizontal but tangential to the slope. As a result, a part of the E_z-field propagates into the recorded electric field, thereby introducing a systematic measurement error that affects the impedance and phase tensor. This error is unrelated to the galvanic and inductive effects defined in Section 2, which are strongest on the extreme points of topography (valleys and peaks). Instead, the magnitude of this error depends directly on E_z and the tilt of the dipoles (i.e the local slope at the receiver location).

To evaluate the effect, pseudo-sections for the ratio of E_z to E_x and E_y,

$$\frac{|E_z|}{\sqrt{|E_x|^2 + |E_y|^2}}, \tag{27}$$

along the two profiles P1 and P2 are given in Fig. 13 together with the slope values calculated in the profile direction. The ratio is practically constant over the plotted period range and it can be seen that E_z reaches significant values on steep slopes (>10°), but for angles smaller than 5° it is smaller than 10 per cent relative to the horizontal component of $\vec{E}$. To assess the effect on recorded transfer functions, we calculated impedances using electric field tangential to the slopes. In this case, the E_z component is coupled into the tilted components,

$$E'_x = E_x \cos(\alpha_x) + E_z \sin(\alpha_x) \tag{28}$$

$$E'_y = E_y \cos(\alpha_y) + E_z \sin(\alpha_y), \tag{29}$$

with the sine of the slope angle α in x- and y-direction at the receiver location. The difference in apparent resistivity and phase between tilted and truly horizontal dipoles is plotted in Fig. 14 as a function of the slope angle in profile direction. Since E_z is small for moderate slope angles (<5°) and due to the multiplication with the sine (eqs 28 and 29), the effect is rather small, reaching only 4 Ωm for ρ_a and 0.01° for ϕ. Given that a slope of 5° results in an altitude difference of 9 m between the electrodes of a 100 m dipole, the effect of tilted dipoles and vertical electric fields can be neglected for most practical scenarios.

5 CONCLUSIONS

In this study, we performed a systematic investigation of the topography effect on MT transfer functions, including the impedance tensor, phase tensor and tipper. We modelled responses with the help of a 3-D high-order finite element modelling code and quantified the effect of real topography over a wide period range (0.01–100 s). Although the exact values depend on a specific topography, we draw a number of conclusions below, which should hold in general.

The responses modelled for real surface undulations revealed the underlying physical processes and showed that topography causes distortions of MT transfer functions due to both galvanic and inductive effects. Galvanic distortions are caused by the charge accumulation across conductivity contrasts. In the presence of topography, charges accumulate on slopes, thereby generating secondary electric fields. Distortions caused by EM induction within and around topographic undulations have a rather complex nature. We showed that in general, inductive effects lead to increased current density in mountain ridges and decreased current density within valleys. We found that inductive effects are strongest at short periods, distorting

Downloaded from https://academic.oup.com/gji/article-abstract/215/3/1943/5101445 by ETH Zürich user on 12 October 2018

amplitude and phase of MT transfer functions, whereas galvanic distortions prevail at long periods, resulting in a static shift effect.

Using real topography from the Hangai Mountains in Mongolia, we found that modelled apparent resistivity values span a range from 12 to 209 Ωm for a 100 Ωm homogeneous subsurface model and phase distortions of -8° to $+13^\circ$ relative to the undistorted values. Apparent resistivities are distorted to higher values in valleys and lower values on mountain tops, phases are distorted in the opposite way. The distortion depends on the local topography gradient. Specifically, the distortions strongly correlate with the steepness and magnitude of the topographic undulations and mountains located more than 5–10 km away from the point of measurement cause virtually no effect in the considered period range (0.01–100 s).

Tippers sense hills and mountains as conductive bodies. For a period of 0.01 s, the real and imaginary parts have an absolute magnitude of up to 0.28, although the effect vanishes a few kilometres away from the topographic features. The long period (100 s) tippers show much smaller effect due to topography, the magnitudes stay below 0.005, and can most likely be neglected for real data which contain noise.

The phase tensor is free of galvanic distortions caused by topography, and therefore remains practically unaffected at long periods, where galvanic effects dominate. For periods <1 s, inductive effects and the 3-D conductivity distribution due to topography affect the phase tensor. It exhibits a notable 2-D influence due to the local topography, whereas the maximum normalized skew angle of $\pm 1.5^\circ$ indicates that 3-D effects remain rather small.

We calculated the effect of vertical electric field for tilted dipoles. Our modelling results suggest that the resulting effect on the impedance is negligible for slope angles of 5° and less.

In summary, galvanic distortions due to topography can be significant and need to be accounted for. In practice, the problem can be alleviated by using the phase tensor and tipper or explicitly inverting for the distortion matrix. Distortions due to inductive effects, which are significant at shorter and intermediate periods, are more difficult to avoid. They can exceed the uncertainties equivalent to a 5 per cent impedance error floor, which is often used in MT inversions. Indeed, a 5 per cent error floor impedance results in a 7 per cent error on the apparent resistivity and 2° on the phase. Disregarding these distortions during the inversion will project the effects of surface topography to the subsurface conductivity structure. The most consistent way to handle these effects is to include the topography in the forward modelling. The increased computational cost is offset by a potential improvement of inversion images and a reduced risk of misinterpretations.

ACKNOWLEDGEMENTS

JSK was supported by SNF DACH program Grant No. 200021L_162660/1. This work was supported by a grant from the Swiss National Supercomputing Centre (CSCS) under project ID767. We want to thank Colin Farquharson and the anonymous reviewer as well as the editor Gary Egbert for their comments and discussion, which helped to improve the manuscript significantly.

REFERENCES

Berdichevsky, M.N. & Dmitriev, V.I., 1976. Distortion of magnetic and electric fields by near-surface lateral inhomogeneities, *Acta Geod. Geophys. Montan. Hung.,* **11,** 447–483.

Berdichevsky, M.N. & Dmitriev, V.I., 2002. *Magnetotellurics in the Context of the Theory of Ill-Posed Problems,* Society of Exploration Geophysicists.

Berdichevsky, M.N. & Dmitriev, V.I., 2008. *Models and Methods of Magnetotellurics,* Springer-Verlag.

Booker, J.R., 2014. The magnetotelluric phase tensor: a critical review, *Surv. Geophys.,* **35**(1), 7–40.

Caldwell, T.G., Bibby, H.M. & Brown, C., 2004. The magnetotelluric phase tensor, *Geophys. J. Int.,* **158**(2), 457–469.

Comeau, M.J. *et al.*, 2018. Evidence for fluid and melt generation in response to an asthenospheric upwelling beneath the Hangai Dome, Mongolia, *Earth planet. Sci. Lett.,* **487,** 201–209.

Grayver, A.V. & Kolev, T.V., 2015. Large-scale 3D geoelectromagnetic modeling using parallel adaptive high-order finite element method, *Geophysics,* **80**(6), E277–E291.

Groom, R.W. & Bahr, K., 1992. Corrections for near surface effects: decomposition of the magnetotelluric impedance tensor and scaling corrections for regional resistivities: a tutorial, *Surv. Geophys.,* **13**(4), 341–379.

Jahandari, H., Ansari, S. & Farquharson, C.G., 2017. Comparison between staggered grid finite-volume and edge-based finite-element modelling of geophysical electromagnetic data on unstructured grids, *J. appl. Geophys.,* **138,** 185–197.

Jiracek, G.R., 1990. Near-surface and topographic distortions in electromagnetic induction, *Surv. Geophys.,* **11**(2), 163–203.

Jones, F.W. & Price, A.T., 1970. The perturbations of alternating geomagnetic fields by conductivity anomalies, *Geophys. J. Int.,* **20**(3), 317–334.

Kordy, M., Wannamaker, P., Maris, V., Cherkaev, E. & Hill, G., 2016. 3-D magnetotelluric inversion including topography using deformed hexahedral edge finite elements and direct solvers parallelized on SMP computers–part I: forward problem and parameter Jacobians, *Geophys. J. Int.,* **204**(1), 74–93.

Ku, C.C., Hsieh, M.S. & Lim, S.H., 1973. The topographic effect in electromagnetic fields, *Can. J. Earth Sci.,* **10**(5), 645–656.

Nam, M.J., Kim, H.J., Song, Y., Lee, T.J., Son, J. & Suh, J.H., 2007. 3D magnetotelluric modelling including surface topography, *Geophys. Prospect.,* **55**(2), 277–287.

NASA JPL, 2013. NASA Shuttle Radar Topography Mission Global 1 arc second, NASA LP DAAC, U.S. Geol. Surv.,.

Ren, Z., Kalscheuer, T., Greenhalgh, S. & Maurer, H., 2013. A goal-oriented adaptive finite-element approach for plane wave 3-D electromagnetic modelling, *Geophys. J. Int.,* **194**(2), 700–718.

Schwarzbach, C., Börner, R.-U. & Spitzer, K., 2011. Three-dimensional adaptive higher order finite element simulation for geo-electromagnetics—a marine CSEM example, *Geophys. J. Int.,* **187**(1), 63–74.

Singer, B.S., 1992. Correction for distortions of magnetotelluric fields: limits of validity of the static approach, *Surv. Geophys.,* **13**(4-5), 309–340.

Usui, Y., 2015. 3-D inversion of magnetotelluric data using unstructured tetrahedral elements: applicability to data affected by topography, *Geophys. J. Int.,* **202**(2), 828–849.

Wannamaker, P.E., Stodt, J.A. & Rijo, L., 1986. Two-dimensional topographic responses in magnetotellurics modeled using finite elements, *Geophysics,* **51**(11), 2131–2144.

APPENDIX: MODELLING RESULTS ALONG P2

Figs A1–A4 show 2-D slices extracted from the 3-D solutions for two selected periods of 0.01 s and 100 s along P2 (see Fig. 3). Note that for the *x*-polarization (eq. 26) primary electric field components are perpendicular to the *xz*-plane shown in Figs A1 and A3, therefore the streamlines of the *x*- and *z*-components of total and secondary electric fields are virtually equal. They are mainly affected by the topography in the *y*-direction. The same holds for the magnetic field due to *y*-polarization (eq. 25) in Figs A2 and A4.

Downloaded from https://academic.oup.com/gji/article-abstract/215/3/1943/5101445 by ETH Zürich user on 12 October 2018

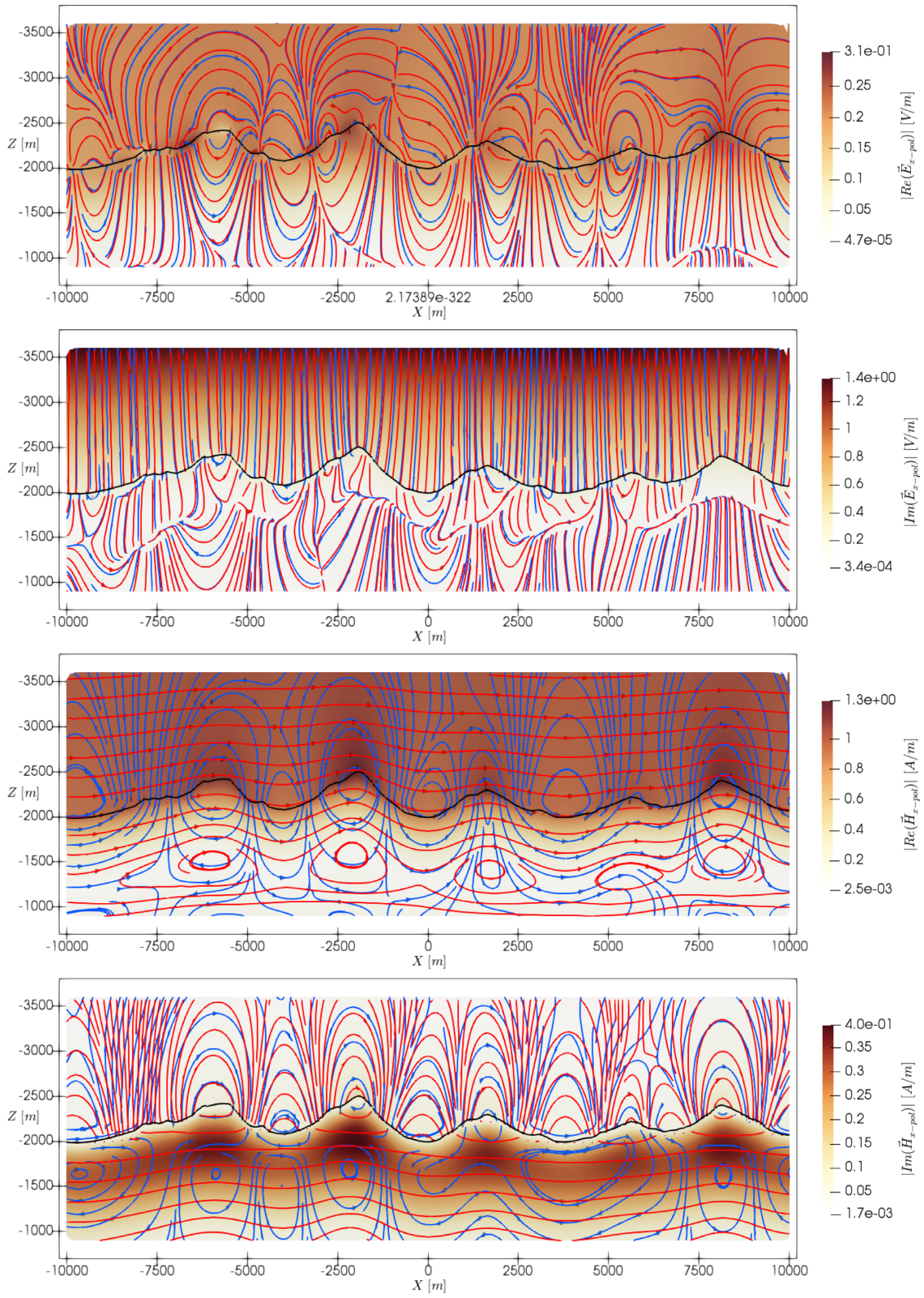

Figure A1. Electric and magnetic fields at the plane along P2 for the *x*-polarized source fields (eq. 26) at the period of 0.01 s. The background colour on all panels show the magnitude of the 3-D vector field and the streamlines represent the direction of the vector field in the *xz*-plane. Red and blue streamlines depict total and secondary fields, respectively.

Downloaded from https://academic.oup.com/gji/article-abstract/215/3/1943/5101445 by ETH Zürich user on 12 October 2018

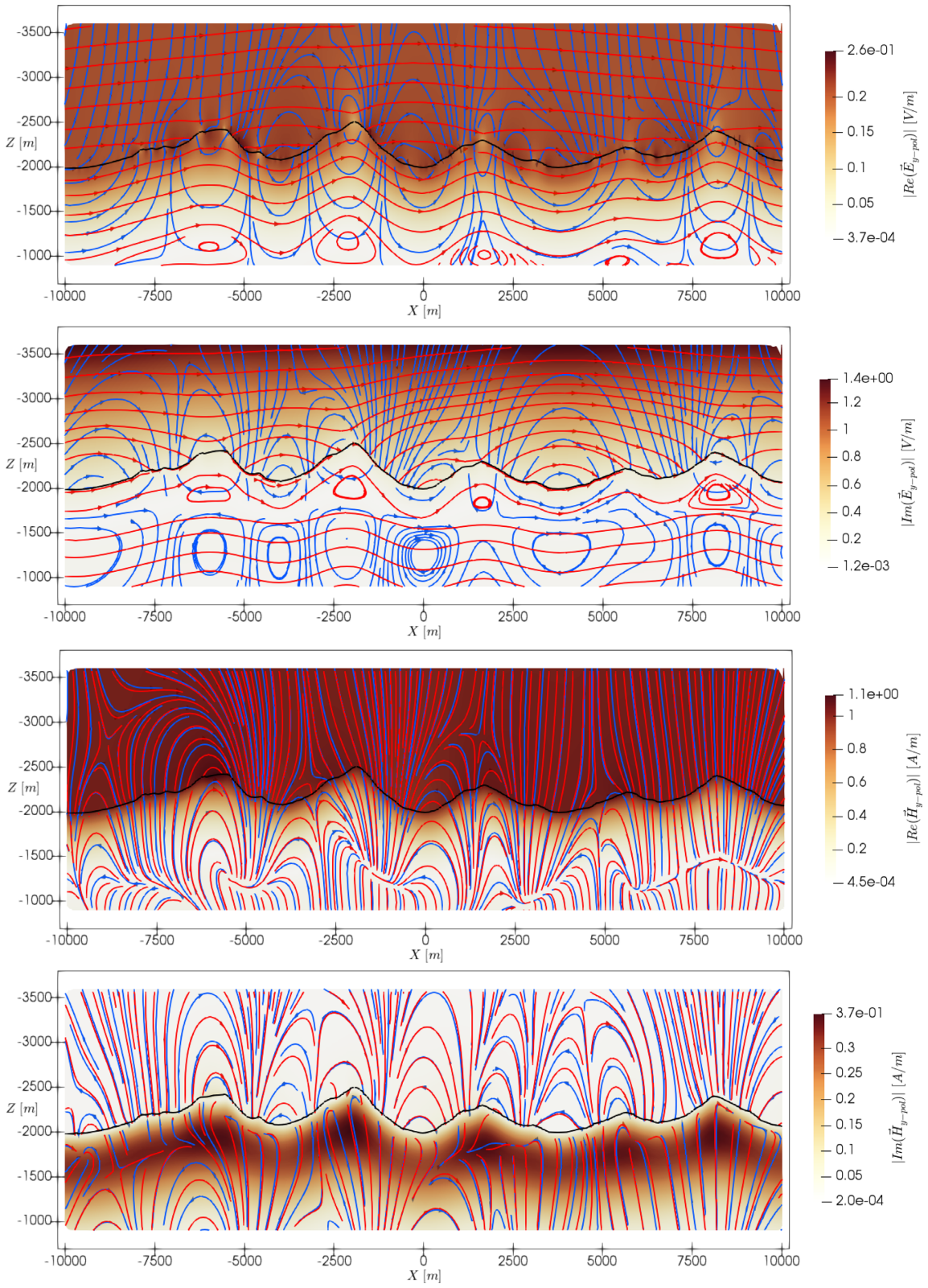

Figure A2. Same as Fig. A1, but for *y*-polarized source fields (eq. 25) at a period of 0.01 s.

Downloaded from https://academic.oup.com/gji/article-abstract/215/3/1943/5101445 by ETH Zürich user on 12 October 2018

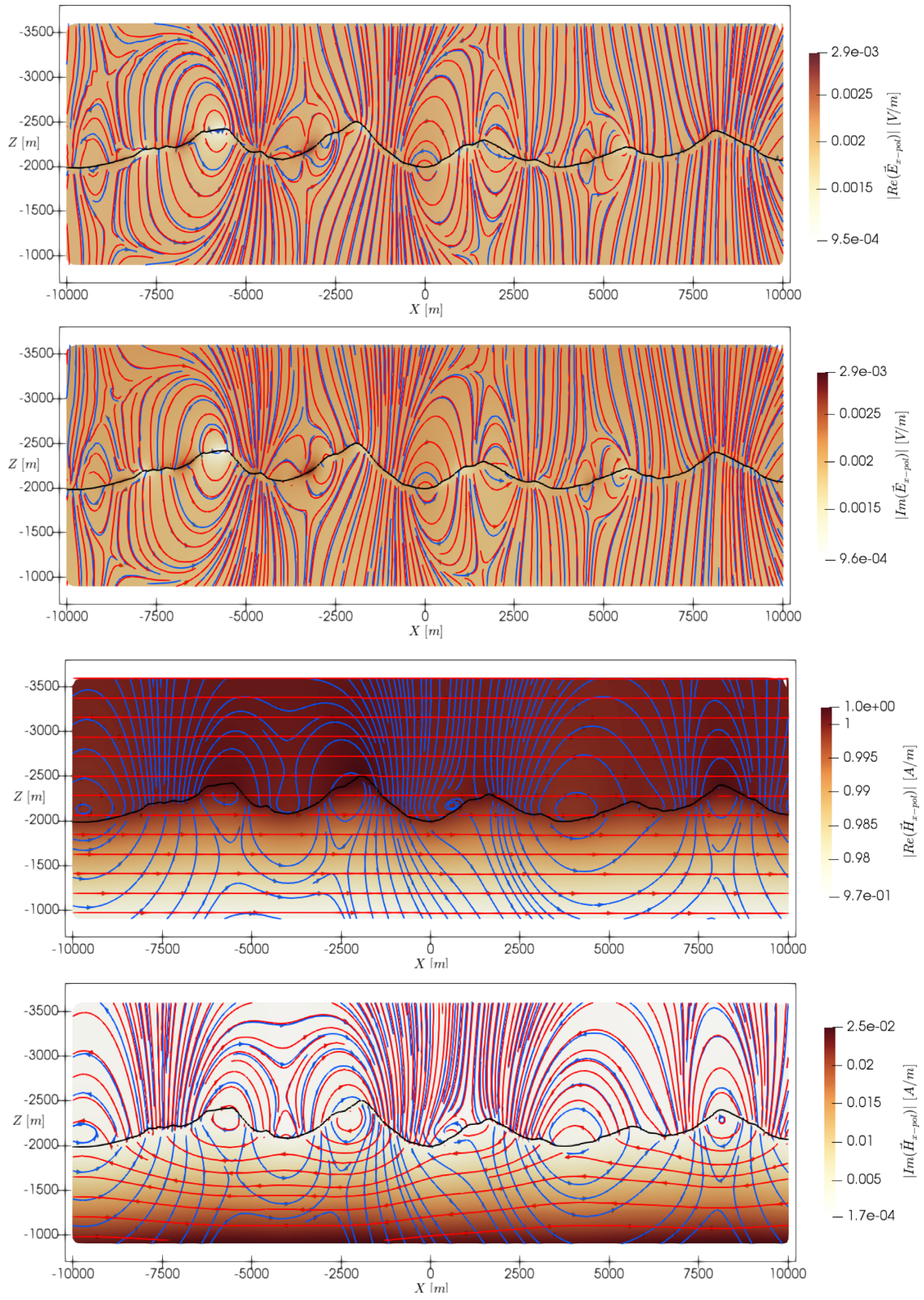

Figure A3. Same as Fig. A1, but for the *x*-polarized source fields (eq. 26) at a period of 100 s.

Downloaded from https://academic.oup.com/gji/article-abstract/215/3/1943/5101445 by ETH Zürich user on 12 October 2018

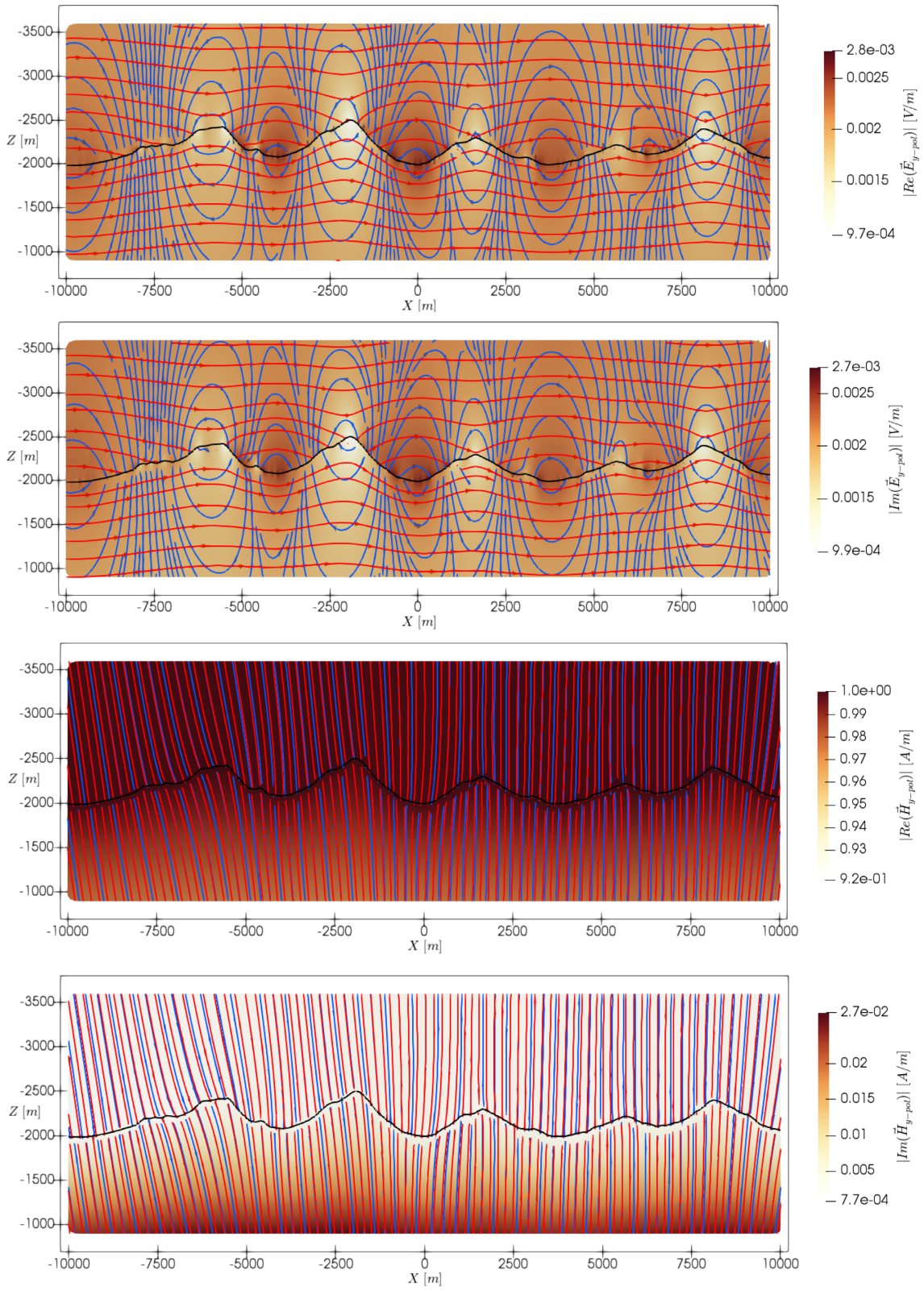

Figure A4. Same as Fig. A1, but for *y*-polarized source fields (eq. 25) at a period of 100 s.

Downloaded from https://academic.oup.com/gji/article-abstract/215/3/1943/5101445 by ETH Zürich user on 12 October 2018